# MICROANALYSIS OF COSMIC DUST:

## *NANOMETER SCALE IMAGING AND ANALYSIS IN THE SEM*

Edward P. Vicenzi

Smithsonian Institution, Museum Conservation Institute, 4210 Silver Hill Road, Suitland, MD 20746, USA

Ed Vicenzi is a research scientist at the Smithsonian Institution's Museum Conservation Institute (MCI). He utilizes a variety of electron, photon, and ion microbeam techniques to study of museum specimens and related materials. Before taking-up his position at MCI he served as the Director of the Analytical Laboratories in the National Museum of Natural History's (NMNH) Department of Mineral Sciences and the co-manager of the Imaging and Analysis Facility at Princeton University. He has served as President and Director of the MicroAnalysis Society (MAS), principal and co-organizer of MAS topical conferences, Chair of the NMNH Senate of Scientists, MAS co-chair for the M&M conference, twice as MAS tour speaker, as well as an organizer for symposia at M&M, AGU, and Goldschmidt conferences. He is the current USA representative for IUMAS, a panel member for science funding agencies, has recently been selected to join the editorial board of a new journal entitled *Heritage Science*, and will serve as Chair for the IUMAS-6 meeting in 2014. Ed is the author or co-author of 50 peer reviewed publications and numerous conference proceedings regarding topics in Earth, planetary, and cultural heritage science. He obtained a PhD from Rensselaer Polytechnic Institute, an MS from the University of Oregon, and a BSc from McGill University, all in Earth Sciences.

## 1. *INTRODUCTION*

Roughly 4.6 billion years ago our solar system's precursor materials were formed from a vast molecular cloud according to astronomical and meteoritical observations and theory. In recent decades some of the best clues regarding this early history were achieved through the study of interplanetary dust particles (IDPs) collected by aircraft in the Earth's stratosphere. The non-terrestrial portion of the particle population represent fragments of both comets and asteroids. IDPs therefore differ from the meteorite collection that represent only asteroids, plus a few larger planetary bodies. IDPs carry valuable information about comets, a class of solar system bodies whose orbits that take them beyond the outer planets. When comets pass through the inner solar system they eject solids owing to volatile ice interaction with intense solar radiation. This interaction forms the well-known visible cometary coma, or tail. Until just a few years ago the study of IDPs has been the only direct link to determining the compositional nature of comets. Recently, we have had the opportunity to examine cometary material with provenance brought back to Earth by NASA's Stardust mission from a known source. The Stardust spacecraft collected thousands of solid particles during a fly-by of comet Wild 2 in 2004 and returned this valuable payload to Earth in 2006 (Figs. 1a and b) [1, 2].

Samples collected in silica aerogel collection tiles have been extracted, sectioned, and examined with a field emission scanning electron microscope (SEM) using scanning transmission electron microscopy (STEM) and scanning transmission X-ray microanalysis by energy dispersive spectrometry (STEM-EDS) in the SEM. Spot analyses of cometary nanoparticles and their matrix collected by beam deflection are presented along with X-ray spectrum imaging results of fine-scale mixtures of cometary materials and aerogel. Strategies for unraveling the complexity of the system using high spatial resolution analysis in the SEM are presented.

## 2. *METHODS*

Particles were identified within aerogel tiles (Figs. 2 a and b) at UC Berkeley by Andrew Westphal and colleagues and extracted using micromanipulation and the keystone method [3]. Flattened keystones containing individual cometary fragments were then embedded in epoxy and ultramicrotomed at NASA's Johnson Space Center (JSC) by Keiko Nakamura-Messenger into slices 70 nm in thickness. Sections were subsequently placed on a carbon film coating a 3.05 mm diameter beryllium grid (Figs. 3 a and b).

Samples were examined using an FEI NanoSEM600. STEM imaging was conducted using FEI's STEM II angularly resolved electron detector, a beam energy of 30 kV, and a working distance of 6.9 mm. Because the STEM and backscattered electron (BSE) detectors share signal amplification electronics dual images cannot be collected in tandem, therefore through-the-lens (TLD) imagery for secondary electron (SE) and BSE modes was used to produce additional image signals to monitor topography and average atomic number at 7 kV. Though the sample was not coated with a conductive film, high vacuum was used for the bulk of the study. A modest water pressure (e.g. ~2 x $10^{-4}$ bar) was used in variable pressure (VP) mode to obtain high resolution VP SEM images with a Helix detector at 2 kV [4, 5].

Compositional analyses were conducted with a 40 $mm^2$ Thermo Fisher Scientific Nano Trace Si(Li) X-ray detector using an electron beam energy of 30 kV and a beam current of 3.25 nA. Data were collected using NSS V2 and processed with both V2 and V3 software. X-ray spectra for point analyses were collected for 50 live seconds. Backgrounds were determined by digital filtering and the Cliff-Lorimer method used to compute specimen composition. Spectrum images were actively corrected for drift every other fame to mitigate the effects of stage and surface charge instability.

## *3. IMAGING STARDUST*

Thin sections for a particle from an off-shoot of the main track (Fig. 2 b), designated by mission nomenclature to be [#C044,2,41,2,0] are the subject of this study. Overview electron images were obtained to map-out the relationship of the embedded particles with respect to holes in the Be grid (Fig. 4a). Unfortunately, the hole density for the Be grids is low, and therefore the probability of having a particle located over a hole is quite low. Bright-field (BF) and high angle annular dark-field (HAADF) imaging at moderate resolutions were used to localize cometary material (Figs. 4 b and c). The impact velocity of the particle relative to the aerogel was 6.1 km/sec, and this velocity was engineered to be significantly reduced as the spacecraft moved in the direction of comet Wild 2's trajectory [6]. Regions of the section rich in cometary particles are typically associated with area of compressed aerogel owing to such impact velocity (Fig. 4d)

Microtome preparation yields high quality 70 nm thick slices allowing for BF, DF, and HAADF imaging, yet sections suffer from artifacts (Figs. 5 a- c). Compression ridges are particularly notable in the BF and SE images in Fig. 5 a. The cometary matter highlighted in in Fig. 5 c imaged at higher resolution shows swarms of spherical to sub-spherical high atomic number (Z) nanoparticles (Fig. 6 a). HAADF image intensity scales approximately with $Z^2$ and is typically unaffected by diffraction effects [7] and is therefore an ideal mode to view the distribution of high Z nanoparticles encapsulated within a lower Z matrix. The largest spheres appear to be complex double-shelled structures where the rims differ in intensity with respect to the particle cores (Figs. 6 a and b). Finally, some regions of the matrix are nearly free of high Z nanoparticles.

## *4. X-RAY MICROANALYSIS OF STARDUST*

*4.1 Improving STEM-EDS*

The angularly resolved STEM detector is capable of obtaining high resolution images in the SEM, however when inserted it serves as a source of X-rays and backscattered electrons beneath the specimen, thereby degrading the analytical results. Dedicated STEM and S/TEM microscopes do not suffer from this design issue, but the addition of STEM ancillary signals in a conventional SEM is generally a more recent addition to the platform. Hence, in order to achieve more accurate X-ray spectra and images, a custom grid holder was designed and fabricated (Fig. 7 a). The Be grid is held within a folded Cu envelope which is then positioned over a hole drilled into an Al disc. The grid/Cu envelope sandwich is kept in place with a stainless steel clip. In an effort to mitigate the effect of backscattered electrons once they have passed through the specimen and re-impacting the specimen a second time from beneath, a ~25 mm long graphite cylinder was placed below the specimen grid (Fig. 7 b). The device efficacy was evaluated by collecting an X-ray spectrum while the beam was positioned over a Be grid hole, distant from the specimen, where the carbon film had been torn away (Fig. 7 c). The hole count spectrum can be regarded as noise and the grid holder geometry suitable for mitigating the influence of back-side BSEs when conducting STEM-EDS analysis.

*4.2 Determining spatial resolution*

No widely-used industry standard is in place for the determination of X-ray lateral resolution. The distance difference between the $84^{th}$ and $16^{th}$ % of the total signal amplitude traced over a "knife edge" interface is one measure that has been utilized by metrologists. A STEM-EDS composite X-ray image shows distinct Fe nanospheres within a silicate matrix. Because the matrix phases contain little Fe, a one dimensional profile across a nanosphere serves as a substitute for an ideal vertical interface (Fig. 8 a). A plot of raw Fe $K_\alpha$ counts as a function of distance from one side of a nanosphere to the other demonstrates that the X-Y resolution for this specimen is ~38 nm, a conservative estimate given the non-planar nature of the

interface (Fig. 8 b). This deep sub 100 nm resolution is within the range (30-60 nm) reported for specimens of similar thickness by Kotula [8].

*4.3 Spot analyses*

Beam deflection was used to collect spectra for focused spot analyses of cometary matter matrix material and high Z nanoparticles (Figs. 9 a and b). Despite the limited size of the activation volume demonstrated above, the scale of microstructural heterogeneity is often smaller than the 70 nm section thickness. As such, not all atoms in the analytical volume are intimately mixed at the atomic scale. Despite this physical constraint one can support the concept of compositional mixing graphically using elemental binary plot relationships. Figures 10 a and b demonstrate that cometary matrix compositions are not pristine, and in fact represent a spread of compositions (Figs. 10 a and b; filled gray ellipses). One end-member of this mixing series is pure silica, the composition of the Stardust aerogel capture medium. The coincidence of the negative correlation between silicon and both sulfur and iron suggest Fe-sulfide could represent the other end-member if one extrapolates the mixing trend to the X axis intercept. Since the spot selection for these analyses were based upon BSE imaging it maybe that single nanometer Fe-sulfides are distributed in three dimensions throughout much of the matrix. Additionally, a distinct high $FeO^{*}$ trend is apparent in figure 10 b (filled dark gray ellipse). Because the associated $SO_3$ values for the data points in the high $FeO^{*}$ trend are all low (1.0 +/- 0.4 1$\sigma$), the most likely end-member for this trend is FeNi metal. In summary, STEM imaging would provide a superior electron imaging mode to select matrix areas for analysis both because of increased spatial fidelity and the ability to view the entire thickness of a section, therefore avoiding zones containing high Z nanoparticles encountered using BSE imaging.

The distribution of compositions for forty seven analyses of high Z nanoparticles is presented with respect to the Fe-S-Ni system (Fig. 11). The vast majority contain less than 10 atom% Ni with a large spread in Fe/S ratio along 2/3s of the Fe-S join and extending nearly to the pure Fe end-member.

*4.4 Spectrum Imaging*

The scale microstructural heterogeneity observed in the STEM imagery of the cometary fragments examined in track 41 is not possible to fully appreciate compositionally using focused beam analyses alone. X-ray spectrum images of were therefore collected to determine the nature and extent of such chemical heterogeneity in two dimensions. Hyperspectral X-ray data were modeled using multivariate statistical (MVS) methods [9] that produce a solution for the X-ray results that yield maximum contrast in the spatial domain [10]. The "spatial simplicity" solution for an overview of a cometary fragment shows the distribution of three dominant components; silica, Mg-bearing silicate, and Fe-rich sulfide/FeNi metal (Figs. 12 a-e). These three components are typical of most areas examined. Both the red and yellow components represent $SiO_2$ where peak ratios differ slightly owing to increased absorption of O X-rays by extra C in the fold of the section. Therefore, the sum of red and yellow pixels denote the regions influenced by the aeogel capture medium while the blue and green regions represent extraterrestrial material. A higher resolution spectrum image (Figs. 13 a-e) show the same results with the addition of an aluminous Mg-silicate component. An alternative method to visualizing Stardust chemical heterogeneity is to output the spectrum imaging results as quantified elemental images (Figs. 14 a-g). While correlations between Fe and S are clear, others (Mg and Si) are less distinct compared to the X-ray hyperspectral output.

## 5. *DISCUSSION AND SUMMARY*

When microstructures like those shown here were first observed by examiners of Stardust specimens, the question was posed as to whether these textures represented a material recognized in IDPs called glass with embedded metal and sulfides, or GEMS [11]. It has since been demonstrated that the fine scale juxtaposition of silica and the wide spread dispersion of Fe-rich nanoparticles are the result of heating and alteration during comet dust capture in aerogel [12-14]. STEM imagery, quantitative point analyses, and X-ray spectrum imaging all support the notion that molten $SiO_2$ admixed briefly with Mg-silicates, Fe sulfides and FeNi metal on a very fine scale ranging from hundreds to tens of nanometers. Loss of S in Fe-rich nanoparticles owing to transient heating can account for the dispersion of compositions indicated by the arrow in Fig. 11. Capture heating as a result of deceleration in aerogel also caused immiscible Fe sulfide encapsulating FeNi metal liquids to form numerous complex nested beads. Fortunately not all Stardust particles captured in aerogel suffered such an ignominious high temperature fate. The interiors of many particles larger than a micrometer, often at the terminus of main tracks, are reported to retain their crystallinity, e.g. unequilibrated olivines and Ca-rich pyroxene have been reported [15]. Impressively, 30 kV imaging and analysis in the SEM can provide information bridging the length scale between bulk analysis in the SEM with thin film results obtained in S/TEM and dedicated STEM instruments.

## 6. *ACKNOWLEDGMENTS*

The author thanks the Stardust curation teams at UC Berkeley and NASA/JSC, specifically Andrew Westphal, Christopher Snead, and Keiko Nakamura-Messenger. Thanks also to Mr. Timothy Gooding and Mr. Timothy Rose at the Smithsonian's NMNH for the fabrication of the custom specimen holder for STEM X-ray microanalysis in the SEM.

## *7. REFERENCES*


1. Brownlee, D.E., *The Stardust Comet Mission: Studying Sediments From The Solar System's Frozen Attic.* Elements, 2012. **8**(5): p. 327-328.
2. Brownlee, D., et al., *Comet 81P/Wild 2 Under a Microscope* Science, 2006. **314**(5806): p. 1711 - 1716.
3. Westphal, A.J., et al., *Aerogel keystones: Extraction of complete hypervelocity impact events from aerogel collectors.* Meteoritics & Planetary Science, 2004. **39**(8): p. 1375-1386.
4. Toth, M., B.L. Thiel, and W.R. Knowles, *Gas Cascade Amplification in Ultra-High-Resolution Environmental Scanning Electron Microcopy.* Microscopy and Microanalysis, 2010. **16**(6): p. 805-809.
5. Toth, M., W.R. Knowles, and B.L. Thiel, *Secondary electron imaging of nonconductors with nanometer resolution.* Applied Physics Letters, 2006. **88**(2).
6. Horz, F., et al., *Impact features on Stardust: Implications for comet 81P/Wild 2 dust.* Science, 2006. **314**(5806): p. 1716-1719.
7. Klein, T., E. Buhr, and C.G. Frase, *TSEM: A Review of Scanning Electron Microscopy in Transmission Mode and Its Applications*, in *Advances in Imaging and Electron Physics, Vol 171*, P.W. Hawkes, Editor. 2012. p. 297-356.
8. Kotula, P.G., *Stem-In-Sem For Medium-Resolution X-Ray Microanalysis.* Microscopy and Microanalysis, 2009. **15**: p. 474-475.
9. Kotula, P.G., M.R. Keenan, and J.R. Michael, *Automated analysis of SEM X-ray spectral images: A powerful new microanalysis tool.* Microscopy and Microanalysis, 2003. **9**(1): p. 1-17.
10. Keenan, M.R., *Exploiting spatial-domain simplicity in spectral image analysis.* Surface and Interface Analysis, 2009. **41**(2): p. 79-87.
11. Bradley, J.P., *Chemically Anomalous, Preaccretionally Irradiated Grains In Interplanetary Dust From Comets.* Science, 1994. **265**(5174): p. 925-929.
12. Bradley, J.P., A.P. Jones, and D.E. Brownlee, *Insight from the unexpected.* Meteoritics & Planetary Science, 2009. **44**(10): p. 1403-1405.
13. Velbel, M.A. and R.P. Harvey, *Sulfide-metal textural relations in an extensively melted stardust grain from comet 81P/wild-2.* Meteoritics & Planetary Science, 2007. **42**: p. A155-A155.
14. Noguchi, T., et al., *Thermal alteration of hydrated minerals during hypervelocity capture to silica aerogel at the flyby speed of Stardust.* Meteoritics & Planetary Science, 2007. **42**(3): p. 357-372.
15. Zolensky, M.E., et al., *Report - Mineralogy and petrology of comet 81P/Wild 2 nucleus samples.* Science, 2006. **314**(5806): p. 1735-1739.

*FIGURE CAPTIONS*

Figure 1. Artist's conception of NASA Stardust mission (a) spacecraft encountering comet Wild 2 with particle collector deployed; (b) aerogel tiles with tracks depicting comet particle impact trajectories. Images courtesy of NASA/JPL.

Figure 2. Visible light imagery of silica aerogel following a cometary particle impact (a) entry site orthogonal to aerogel collector tile surface; (b) profile of track 41/tile 44 (length ~ 11 mm). Image courtesy of Andrew Westphal, UC Berkeley.

Figure 3. (a) Diagram illustrating the sample and substrate stack prepared for imaging and analysis; b) Reflected light (RL) image of slices of epoxy and particle-aerogel composites on a beryllium grid with particle of interest (black circle) over ~75 μm diameter hole. RL image courtesy of Keiko Nakamura-Messenger, NASA JSC.

Figure 4. SEM-based image magnification series depicting quadrilateral-shaped slices of epoxy and particle-aerogel composites on a beryllium grid. (a) Through-the-lens (BSE mode) overview of specimen surfaces; (b-d) STEM HAADF images showing (b) multiple holes in Be grid at moderate magnification; (c) a section of particle-aerogel and folded C film over a single grid hole; and (d) cometary matter and compressed silica aerogel (white arrow).

Figure 5. HAADF imagery of particle section in Fig, 3 (a) bright-field image depicting ultra microtome artifacts (black arrows). Inset: TLD SE image showing specimen topography; (b) dark-field and; (c) high angle annular dark-field images.

Figure 6. Images of cometary matter at high resolution; (a) HAADF image showing dispersed high Z nanoparticles, inclusion-free regions, and vesicles. Inset: Helix image showing surface topography; (b) BF image unrelated to (a). Multi-shelled spheres in both images (a) and (b) are highlighted (white circles).

Figure 7. Custom holder for STEM X-ray microanalysis in the SEM (a) Cu grid holder and stainless steel clip on a 25 mm round Al disc; (b) graphite cylinder positioned below TEM grid; (c) X-ray spectrum collected over hole in C film/Be grid.

Figure 8. (a) Composite raw count X-ray image (red-Si;green-Fe;blue-Mg), unfilled yellow arrow shows location of line profile; (b) one dimensional intensity profile across Fe-rich nanoparticle (step-size = 9.4 nm).

Figure 9. BSE images with superimposed spot X-ray spectra (nested white circles) collected using beam deflection. (a) spectrum from a particle-free region; (b) spectrum representative of Fe-rich nanoparticles.

Figure 10. X-Y scatter plots for matrix regions expressed as weight per cent (a) $SiO_2$ *versus* $SO_3$; (b) $SiO_2$ *versus* $FeO^*$ (total Fe). Filled red circle represents pure silica aerogel.

Figure 11. Ternary scatter plot in the sulfur-iron-nickel system for Fe-rich nanoparticles on an atom basis.

Figure 12.(a) Composite overlay of MVS component images (red- Si-rich; green- FeS-rich; blue- SiMg-rich; yellow- Si-rich).(b-e) associated images and spectra for red, green, blue, and yellow components. Note: component image and spectrum representing epoxy not shown.

Figure 13.(a) High resolution composite overlay of MVS component images (red- Si-rich; green- FeS-rich; blue- SiMg-rich; yellow- SiAlMg-rich).(b-e) associated images and spectra for red, green, blue, and yellow MVS components.

Figure 14. Quantified elemental images (atom per cent) of cometary matter at high resolution superimposed upon a BSE image (a) HAADF image of same area shown in Fig. 13; (b) Fe; (c) Al; (d) Mg; (e) S; (f) Si; (g) O. False-color intensity scale shown with an intensity threshold of 0.5 at %.

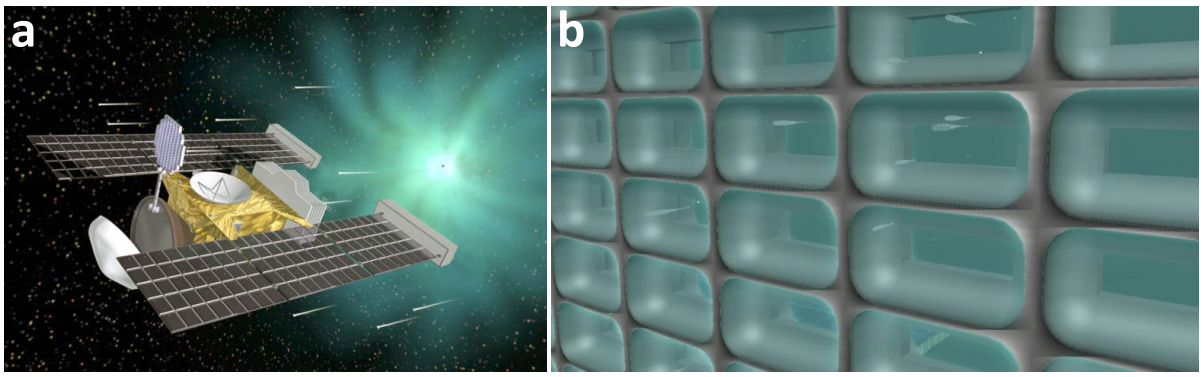


Figure 1.


Figure 2.

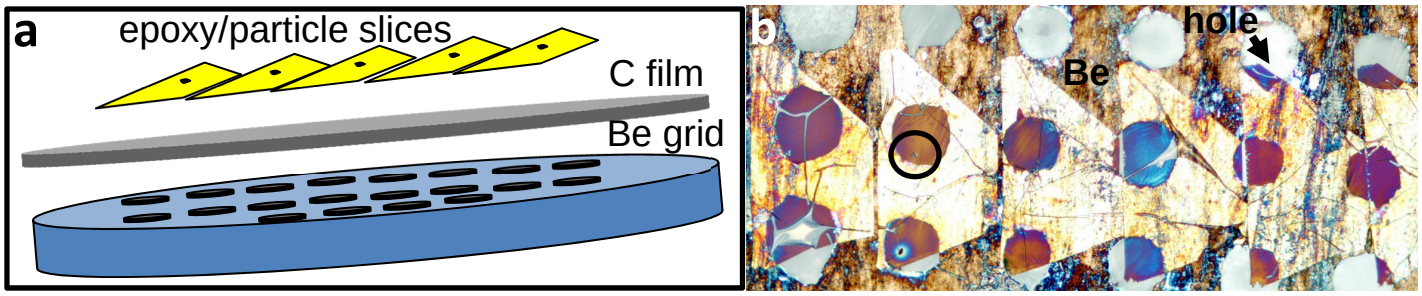


Figure 3.

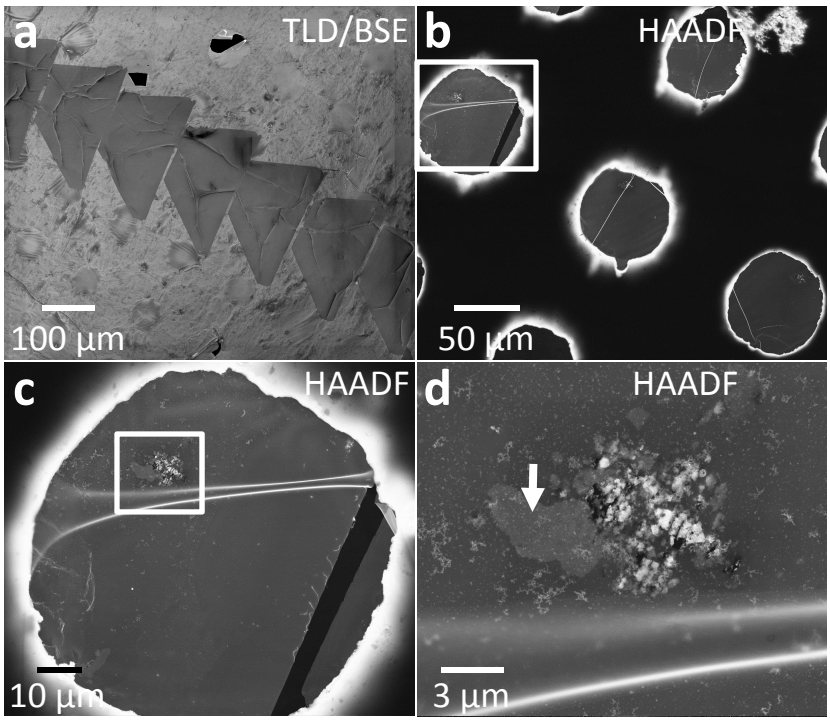


Figure 4.

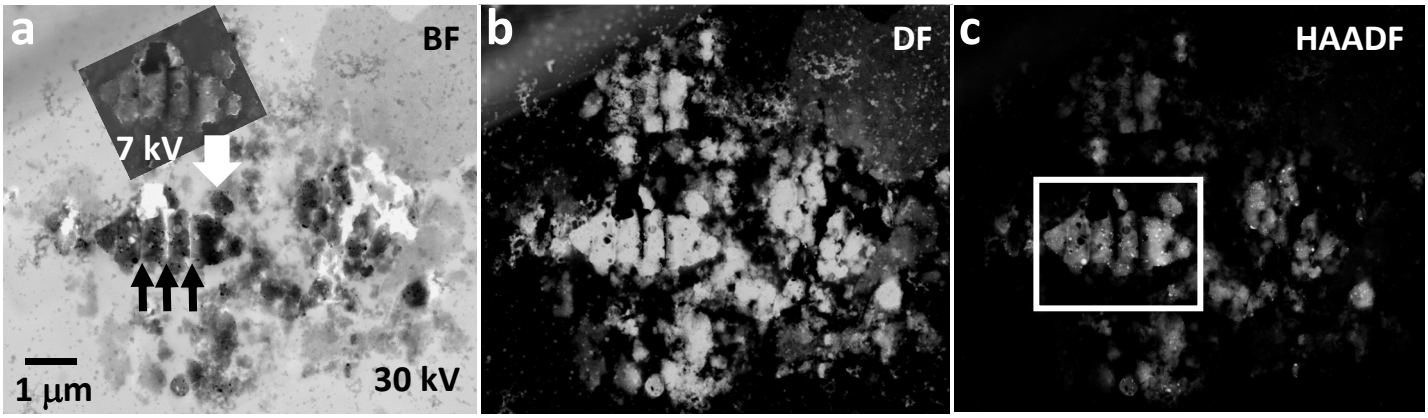


Figure 5.

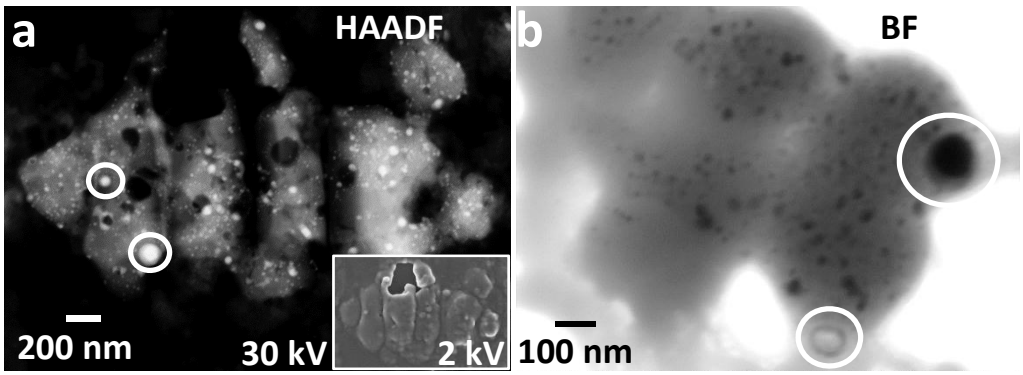


Figure 6.

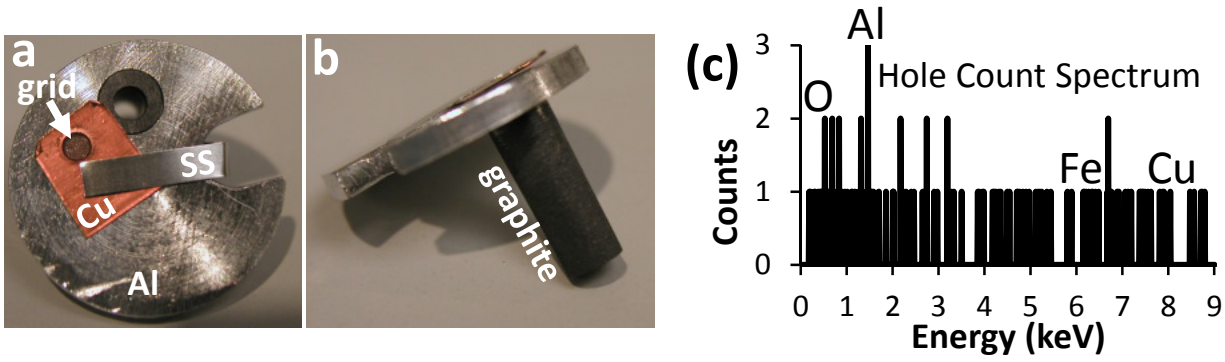
a
grid
SS
Cu
Al
b
graphite
(c)
Al
O
Hole Count Spectrum
Fe
Cu
Counts
0
1
2
3
0 1 2 3 4 5 6 7 8 9
Energy (keV)

Figure 7.

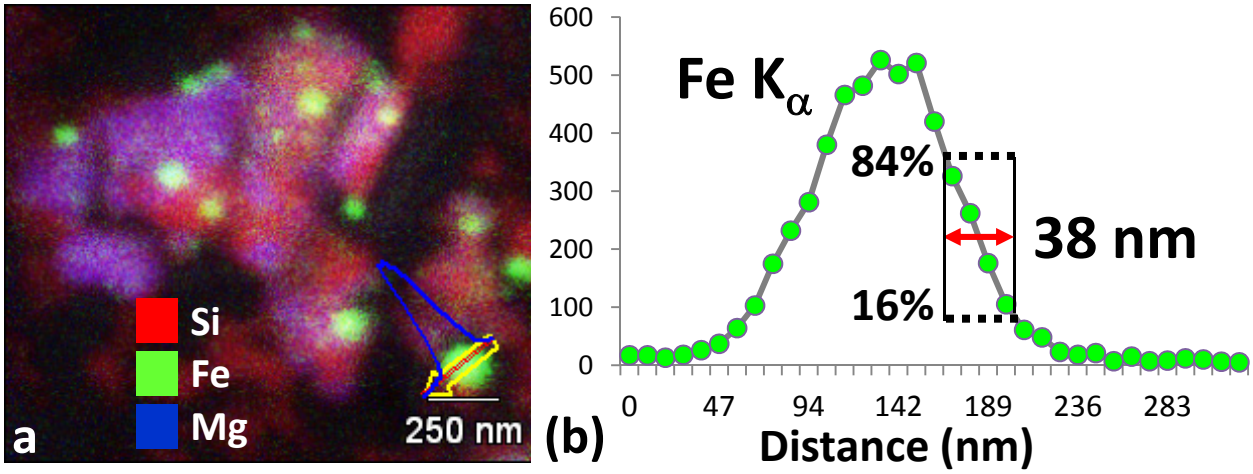
Si
Fe
Mg
250 nm
a
(b)
Fe Kα
84%
16%
38 nm
600
500
400
300
200
100
0
0
47
94
142
189
236
283
Distance (nm)

Figure 8.

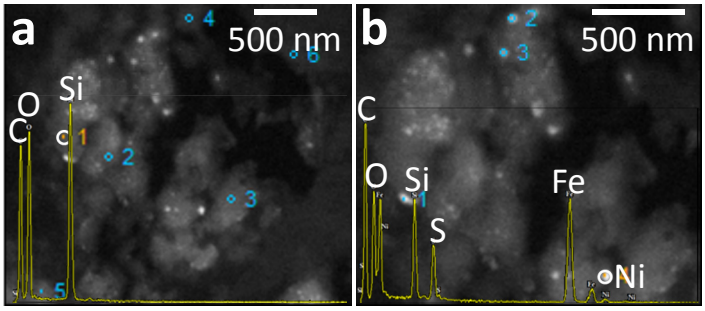


Figure 9.

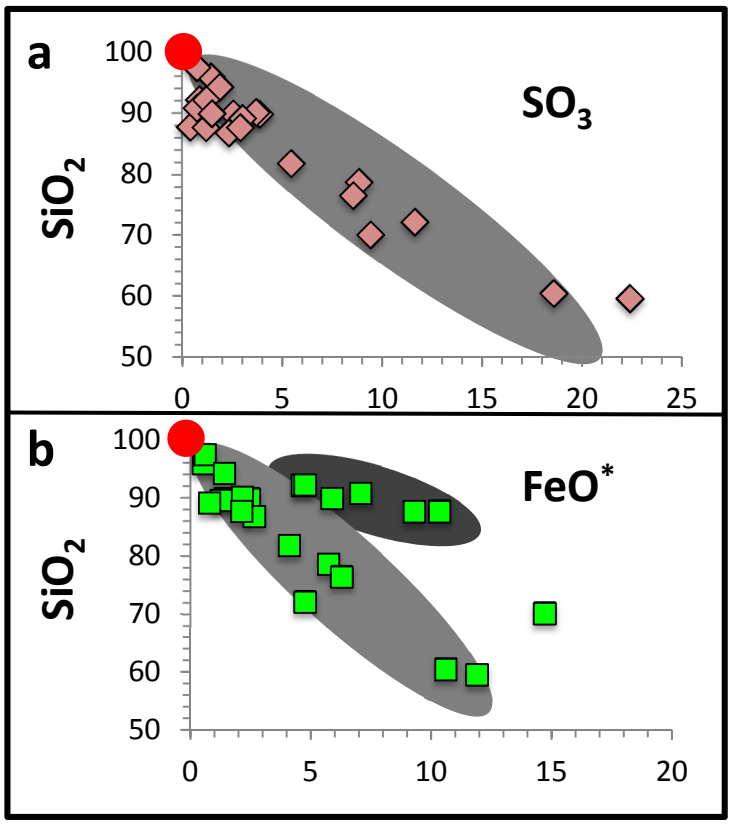
a
100
90
80
70
60
50
SiO2
SO3
0
5
10
15
20
25
b
100
90
80
70
60
50
SiO2
FeO*
0
5
10
15
20

Figure 10.

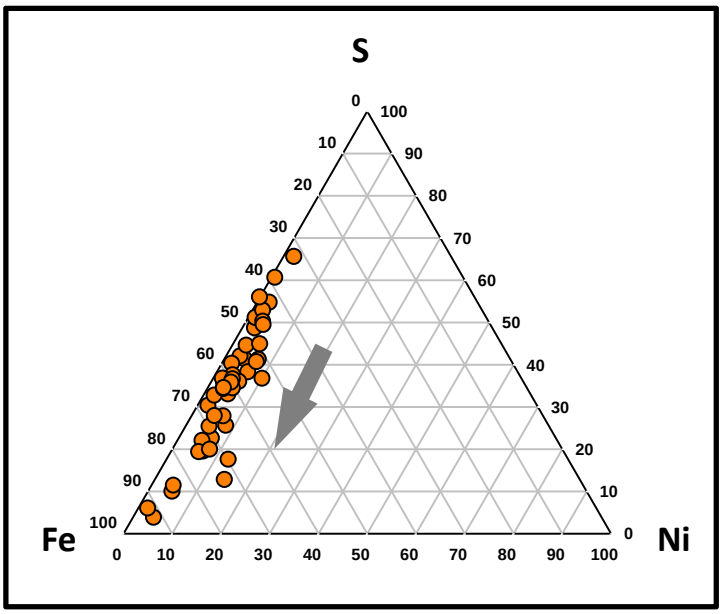


Figure 11.

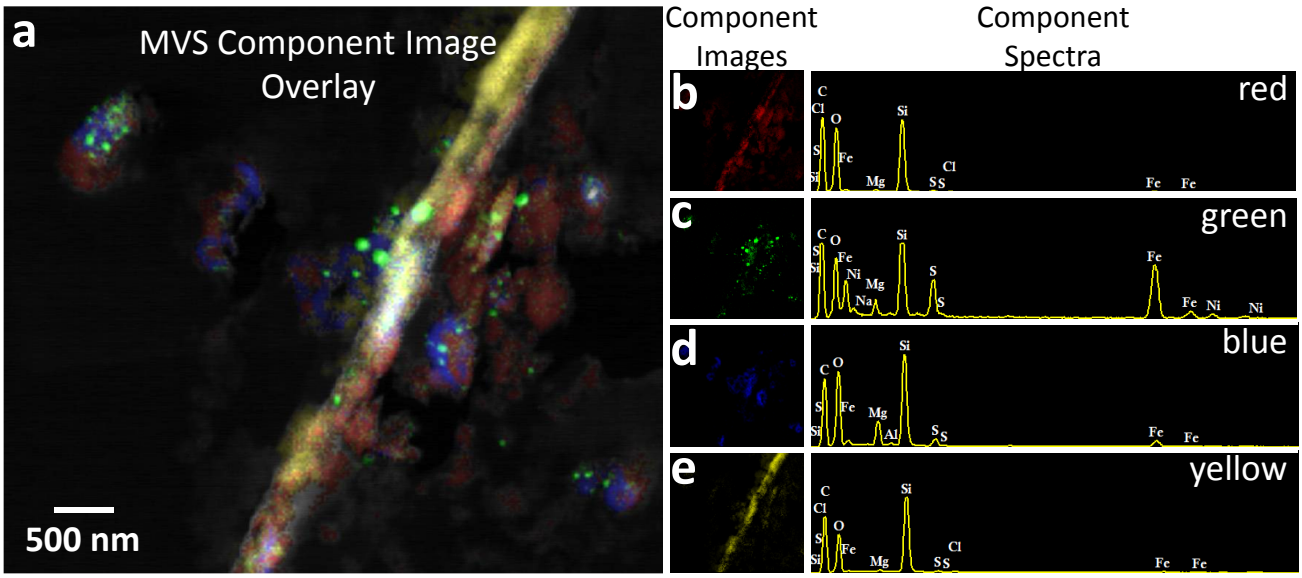
a
MVS Component Image Overlay
500 nm
Component Images
Component Spectra
b
red
c
green
d
blue
e
yellow

Figure 12.

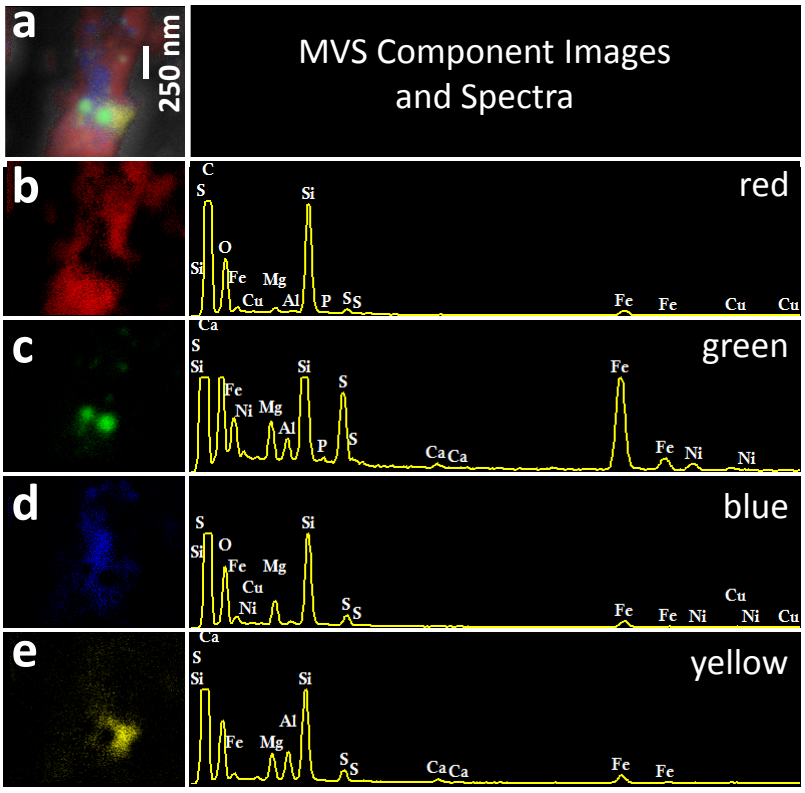
a
250 nm
MVS Component Images
and Spectra
b
red
c
green
d
blue
e
yellow

Figure 13.

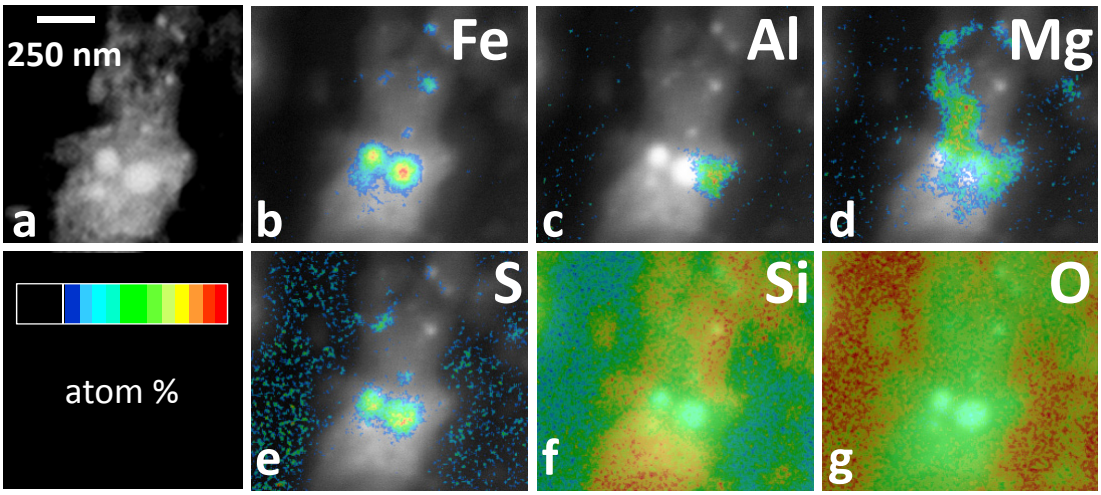


Figure 14.